

This is the accepted manuscript made available via CHORUS. The article has been published as:

# Raman spectroscopy and electrical transport studies of free-standing epitaxial graphene: Evidence of an AB-stacked bilayer

Shriram Shivaraman, Johannes Jobst, Daniel Waldmann, Heiko B. Weber, and Michael G. Spencer

Phys. Rev. B **87**, 195425 — Published 13 May 2013

DOI: [10.1103/PhysRevB.87.195425](https://doi.org/10.1103/PhysRevB.87.195425)

# Raman Spectroscopy and Electrical Transport Studies of Free-Standing Epitaxial Graphene: Evidence of an AB stacked Bilayer

*Shriram Shivaraman,<sup>†, §, \*</sup> Johannes Jobst,<sup>‡, §, \*</sup> Daniel Waldmann,<sup>‡</sup> Heiko B. Weber,<sup>‡</sup> and  
Michael G. Spencer<sup>†</sup>*

<sup>†</sup>School of Electrical and Computer Engineering, Cornell University, Ithaca, NY 14853, USA  
and <sup>‡</sup>Lehrstuhl für Angewandte Physik, Universität Erlangen-Nürnberg, 91058 Erlangen,  
Germany.

KEYWORDS. Epitaxial graphene, free-standing, Raman, magnetotransport, AB stacking,  
Bilayer

ABSTRACT. We fabricate free-standing graphene structures from epitaxial graphene on silicon carbide using a photoelectrochemical (PEC) etching process. A combination of Raman spectroscopy and magnetotransport measurements was used to investigate multi-terminal devices in various geometries. From the analysis of Raman data and Shubnikov-de Haas oscillations we conclude that the buffer layer is converted into a graphene layer and thus, monolayer graphene on SiC gets converted to a free-standing AB-stacked bilayer. The bilayer exhibits inversion-symmetry breaking because of differential doping between the layers. Additionally, lateral

inhomogeneities exist in the form of domains with non-uniform mobility. The same PEC process on a pure buffer layer, however, does not yield monolayer graphene.

## I. INTRODUCTION

Epitaxial graphene (EG) on silicon carbide (SiC) is a promising candidate for wafer-scale graphene-based electronics.<sup>1</sup> Therefore, the structural, electronic and optical properties of EG have been investigated in several studies.<sup>2,3</sup> It is observed that few-layer EG can be grown epitaxially on the Si-face of on-axis SiC, and that the graphene layers are AB-stacked (Bernal type).<sup>4</sup> In addition, scanning tunneling microscopy and electron diffraction experiments<sup>2</sup> have revealed the presence of a buffer layer below the first graphene layer. The buffer layer, also called the zeroth layer, is composed entirely of carbon atoms and has a  $(6\sqrt{3}\times 6\sqrt{3})R30^\circ$  reconstruction on the (0001) Si-face of SiC. It is electrically insulating and angle-resolved photoemission spectroscopy (ARPES)<sup>2</sup> has established the band structure of this layer to be non-graphene-like. However, at elevated temperatures, hydrogen,<sup>2</sup> fluorine,<sup>5</sup> or gold<sup>6</sup> intercalation can transform the buffer layer into a graphene layer. In particular, hydrogen<sup>2,7</sup> and oxygen<sup>8</sup> intercalation studies of monolayer EG confirm that upon intercalation, the buffer layer is converted to a graphene layer and the multi-band electronic structure of AB stacked bilayer graphene is observed.

The interaction of graphene with the substrate causes a reduction of the charge carrier mobility  $\mu$ .<sup>7</sup> It has been shown that this coupling can be reduced by the intercalation procedures described above. However, the achieved mobilities in this quasi-freestanding monolayer graphene (QF-MLG)<sup>7</sup> and quasi-freestanding bilayer graphene (QF-BLG)<sup>9,10</sup> are well below the values observed for suspended exfoliated graphene, devoid of any substrate interactions.<sup>11</sup> It is thus

desirable to investigate similar free-standing epitaxial graphene (FSEG) structures electrically. Doubly-clamped FSEG bridges were previously produced using a photoelectrochemical (PEC) technique to etch away the SiC substrate.<sup>12</sup> Their mechanical properties were studied, but electrical transport measurements in these devices have been challenging and have not been reported so far. In this work, we use a combination of electrical transport measurements and Raman spectroscopy to study FSEG devices. We find that when we start with a nominally monolayer EG, the FSEG exhibits properties characteristic of an AB-stacked bilayer graphene. We hypothesize that during the etching process, the buffer layer converts to a graphene layer, in a fashion similar to the intercalation methods mentioned earlier, and causes the formation of a graphene bilayer. The bilayer graphene so formed, however, is electronically very inhomogeneous. In addition, we observe mechanical failure of the free-standing buffer layer (probably due to presence of defects or tensile strain<sup>7</sup>) if it is not supported by a graphene layer. Therefore, no freestanding monolayer of epitaxial graphene could be produced. However, the PEC etching of buffer layer samples reveals a method for the production of suspended graphene nanoribbons (see Supplemental Material for details).

## II. DEVICE FABRICATION

For the PEC etching process, it is important that the graphene is grown on an electrically conductive substrate, whereas for electrical characterization, the substrate needs to be insulating. We, therefore, used three types of substrates: semi-insulating SiC implanted with nitrogen rendering it n-type close to the surface, semi-insulating SiC implanted with aluminum rendering it p-type, and bulk n-type SiC. In the former two substrates, the implanted conductive region is chosen such that it is removed completely during the PEC etch, leaving behind only insulating

SiC. The latter becomes insulating below  $\sim 70\text{K}$  when the nitrogen dopants freeze out. Here, we report on results obtained using devices on the bulk n-type SiC substrate because electrostatic discharge during contacting or mounting of the samples caused most of the devices on insulating SiC to rupture. Details about FSEG devices on the semi-insulating substrates are given in the Supplemental Material. EG devices were fabricated on the hydrogen etched Si-face of 6H-SiC substrates by thermal decomposition at  $1750^\circ\text{C}$  under 1 bar of argon atmosphere following the process described in Emtsev et al.<sup>1</sup> For the buffer layer samples, the growth temperature was reduced to  $1450^\circ\text{C}$ . The structures were patterned using electron-beam lithography where the PMMA resist served as etch mask during the oxygen-plasma process employed to pattern the graphene. The contact areas were fabricated by evaporation of Ti/Au (5nm/50nm) and lift-off technique. A subsequent PEC etch of the SiC in a 2% aqueous potassium hydroxide (KOH) electrolyte created the undercut to form FSEG devices. The SiC die with the patterned EG devices served as the anode of a home-built Teflon electrochemical cell having a platinum sheet as the counter electrode. The electrochemical cell was placed under the objective of an epifluorescence microscope equipped with a 100 W mercury arc lamp, which acted as the source of UV light. A voltage of 700-900 mV was applied for the duration of the etch, which lasted for  $\sim 2$  hours. A peristaltic pump was used to ensure circulation of the electrolyte during the etch. Typical SiC etch rates were  $1\text{-}2\ \mu\text{m/hr}$ . Afterwards, the devices were dried using a carbon dioxide-based critical point dryer. We also fabricated large-area Hall bars and studied the transport properties after exposing them to the PEC etching conditions. This was performed to investigate if the PEC etching process had an adverse effect on the graphene. We first mention the transport measurements in the large area Hall bars and then discuss the FSEG devices.

### III. RESULTS AND DISCUSSION

#### A. Effect of PEC etching conditions on transport properties

In order to investigate the impact of the PEC etching on the transport properties, large-area Hall bars (1000x200 $\mu\text{m}$ ) were fabricated, in order to avoid underetching. One Hall bar was studied directly after preparation ( $n = 7.8 \cdot 10^{12} \text{ cm}^{-2}$ ,  $\mu = 820 \text{ cm}^2/\text{Vs}$ ); one was immersed in KOH solution for 1.5 hours with a voltage of 900 mV applied ( $n = 4.6 \cdot 10^{12} \text{ cm}^{-2}$ ,  $\mu = 1250 \text{ cm}^2/\text{Vs}$ ); the third one was exposed to ultraviolet (UV) light in addition to KOH and the applied voltage ( $n = 3.9 \cdot 10^{12} \text{ cm}^{-2}$ ,  $\mu = 1670 \text{ cm}^2/\text{Vs}$ ). From the transport measurements, we conclude that the PEC etching has no negative effect on the mobility (the increased mobility is probably related to the decrease of  $n$ , which might be either a doping or an ageing effect). Moreover, evaluation of weak-localization data confirms that the intervalley-scattering length<sup>13,14</sup>  $l_{iv} \approx 95 \text{ nm}$  – the average length between two short range scatterers – is similar for all three devices. Consequently, no additional (short-range) defects are created by the PEC treatment in the non-underetched Hall bars.

#### B. FSEG devices on n-type SiC

Fig. 1 shows examples of two-terminal and multi-terminal FSEG devices produced using the PEC etching technique. It is possible to obtain large free-standing devices spanning several tens of microns as demonstrated by the Hall bar in Fig. 1(b). Sometimes, tears were seen, indicated by the arrows in Fig. 1(a). It is unknown if these were present originally in the grown graphene or were developed during the etching process. In addition, small patches with bright contrast (shown encircled in Fig. 1(a)) were observed occasionally below the graphene in the SEM

images. These have been identified as SiC residue using energy-dispersive X-ray spectroscopy (EDX).<sup>15</sup>

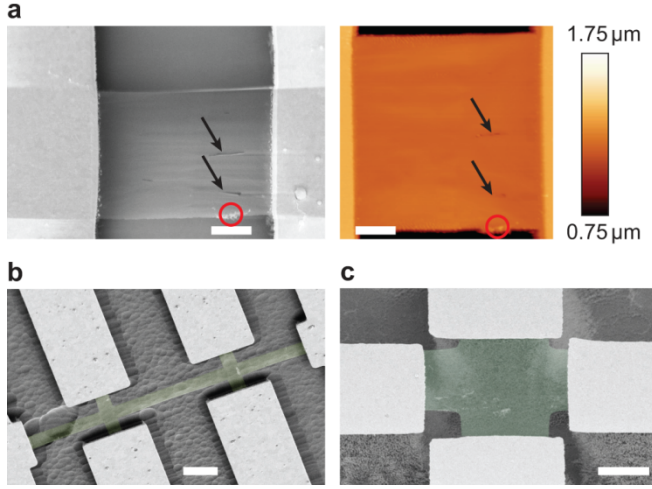


**Figure 1.** Scanning electron microscope (SEM) and atomic force microscope (AFM) images of two-terminal and multi-terminal FSEG devices. (a) Two-terminal device. Left: SEM image taken using a  $45^\circ$  angle stage. Right: AFM image. Scale bars – 1  $\mu\text{m}$ . Tears are visible in the device and are indicated by arrows. The circle marks the location of SiC residues, which are left behind after the etch. (b) Multi-terminal device in Hall bar geometry. Graphene is shown in false color for improved contrast. Scale bar – 5  $\mu\text{m}$ . (c) Multi-terminal device in Hall cross geometry. Scale bar – 2  $\mu\text{m}$ .

### C. Raman spectroscopy of FSEG devices

Fig. 2(a) shows Raman spectra of the graphene on SiC substrate and the free-standing devices obtained using a confocal Raman microscope with a  $100\times$  (N.A. 0.9) objective and a laser excitation of 488 nm (argon-ion laser). The FSEG devices showed G and 2D bands characteristic of graphene.<sup>16,17</sup> The G peak is associated with the doubly degenerate zone-center longitudinal

and in-plane transverse optical phonon (LO and iTO) modes. The 2D peak corresponds to a two-phonon excitation associated with the zone-boundary iTO phonons and has been found to have unique signatures distinguishing layer number and stacking order for few-layer graphene systems.<sup>18</sup> A small D peak, which corresponds to the zone-boundary iTO phonon, was also seen in some cases and may be activated by defects. Compared to EG on SiC, the G and 2D peaks of FSEG are red-shifted, indicating that the compressive strain present in the graphene on the substrate is released after suspending the structures.<sup>12</sup> In addition, the signal strength of the peaks was enhanced in the FSEG devices and little background from the second-order SiC Raman peaks<sup>19,20</sup> was detected, confirming the suspended nature of the devices.

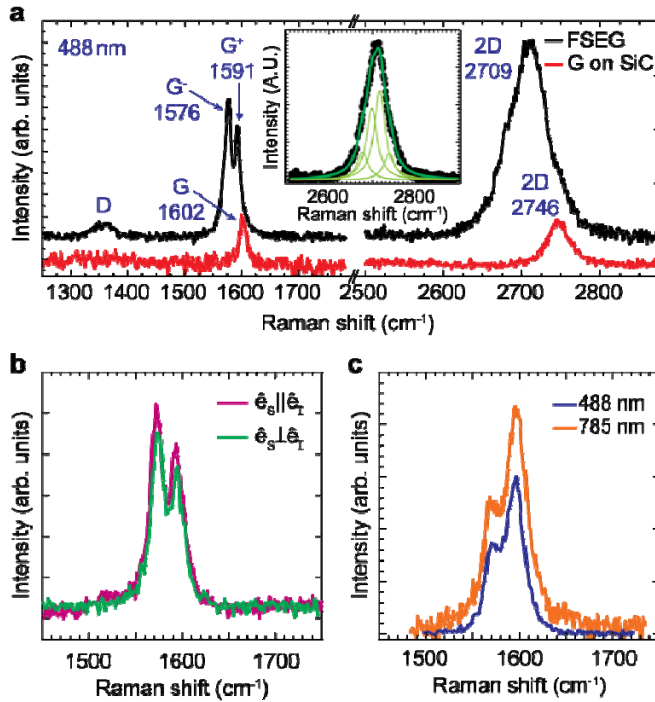


**Figure 2.** (a) Raman spectra using 488 nm excitation for FSEG (black) and graphene on SiC substrate (red). Background from the SiC Raman modes has been subtracted. The G, 2D and D bands are indicated. Red-shifts in the FSEG bands are apparent. Inset shows 2D band of FSEG fit using four Lorentzians of FWHM 30 cm<sup>-1</sup>. (b) Polarization-dependent Raman spectra of



FSEG. Pink (green) curve shows G band when the polarization of scattered light,  $\hat{e}_S$ , is parallel (perpendicular) to that of incident light,  $\hat{e}_I$ . (c) Raman spectra of FSEG using two different excitation energies – 488 nm (2.54 eV, blue) and 785 nm (1.58 eV, orange). No dispersion was observed.

Closer observation reveals that the lineshape of the broad G mode in FSEG could be approximated very well as a sum of two Lorentzian components. In fact, spatial Raman mapping revealed explicit splitting of the G mode over most area of the devices. We discuss next four possible reasons for the splitting of the G band. First, uniaxial strain in monolayer graphene may cause the G band to split into two components denoted by  $G^+$  and  $G^-$  ( $G^+/G^-$  denotes the higher/lower energy component of the G peak).<sup>21,22</sup> For graphene under uniaxial strain, the intensities of the  $G^+$  and  $G^-$  modes have a sinusoidal dependence on the angle between incident and scattered polarizations. Thus, the lineshape would be expected to differ significantly for light scattered along orthogonal polarizations.<sup>21,22</sup> Fig. 2(b) displays Raman spectra acquired with  $\hat{e}_S$  parallel and perpendicular to  $\hat{e}_I$ , where  $\hat{e}_S$  and  $\hat{e}_I$  denote the polarization vector of scattered and incident light respectively. We see no observable dependence of the G band lineshape on the polarization direction. In addition, for uniaxially strained graphene, both  $G^+$  and  $G^-$  modes would simultaneously red-shift (tensile strain) or blue-shift (compressive strain). However, in FSEG the  $G^+$  and  $G^-$  modes shifted in opposite directions from the zero-strain position of  $\sim 1580 \text{ cm}^{-1}$ . Thus, the model of uniaxial strain in monolayer graphene does not explain the observed splitting of the G mode.

A second possibility is chemical modification or introduction of defects in the graphene. This causes the appearance of the defect-activated D' band in graphene at  $\sim 1620 \text{ cm}^{-1}$ , which

corresponds to an intra-valley scattering event due to a LO phonon<sup>17</sup> and could lead to an apparent modification of the G peak lineshape. However, the position of the observed  $G^+$  peak is much below  $1620\text{ cm}^{-1}$ . Secondly, because of the larger electron-phonon coupling for the zone-boundary  $\Gamma$ TO branch in graphene, the intensity of the D peak would be higher than the D' peak,<sup>23</sup> which is not true in our case. In addition, unlike the D' peak<sup>24</sup>, the  $G^+$  mode does not exhibit any dispersion with excitation energy, as shown in Fig. 2(c). Thus, we unambiguously discount the D' mode as an explanation. Third, a splitting of the G band due to symmetry breaking by molecules<sup>25</sup> in monolayer graphene is also eliminated as a possibility because the 2D peak width in FSEG is much larger than that expected for monolayer graphene.

Fourth, and in keeping with the recent demonstrations of quasi-free-standing epitaxial graphene by various intercalation procedures,<sup>2,5,6,8</sup> we offer an interpretation of our observations by hypothesizing the conversion of monolayer-EG into a free-standing bilayer after the PEC etching process. It has been confirmed by ARPES that hydrogen intercalation converts monolayer EG grown on top of the buffer (zeroth) layer into AB stacked bilayer graphene.<sup>2</sup> Thus, it is reasonable to assume that the bilayer graphene obtained after the PEC etching process is also AB stacked.<sup>9</sup> The splitting of the G peak in Bernal stacked bilayer graphene can be a consequence of inversion symmetry breaking.<sup>26--29</sup> Breaking of inversion symmetry may be caused by different charge carrier concentrations in the top and bottom layers.<sup>23,26,27,30--33</sup> In AB stacked bilayer graphene, the phonon modes of the top and bottom layers are coupled. There are two phonon modes at the zone center – one corresponding to the in-phase (IP) motion of atoms in the two layers and another corresponding to an out-of-phase (OP) motion. In pristine bilayer graphene, only the IP mode having even parity is Raman active and corresponds to the single G peak; the OP mode is infrared active because of odd parity. When inversion symmetry is

removed, the new phonon eigenstates of bilayer graphene are superpositions of the original IP and OP modes. Thus, both of the new eigenmodes become Raman active because of the even symmetry IP component. This explains the splitting of the G peak into  $G^+$  and  $G^-$  modes. In accordance with observations, for certain doping levels, the  $G^+$  and  $G^-$  modes may straddle the pristine bilayer G peak at  $\sim 1580 \text{ cm}^{-1}$ .<sup>28</sup> Similar splitting has been reported for QF-BLG after oxygen intercalation.<sup>8</sup> Further support for the coupled bilayer hypothesis comes from comparison of the 2D peak before and after the PEC etch. The 2D peak of the FSEG devices is broader – full-width at half-maximum (FWHM)  $56 \text{ cm}^{-1}$  vs  $31 \text{ cm}^{-1}$  for graphene on SiC – and may, in fact, be fit by multiple Lorentzians (see inset of Fig. 2(a)). It has been shown that, in case of bilayer graphene, high doping can lead to a broad 2D peak with indistinct and/or reduced splitting because of electron-electron correlation effects,<sup>34,35</sup> which may explain the differences between the 2D peak lineshape of FSEG and exfoliated bilayer graphene, where the 2D peak splitting is more explicit.

In order to investigate the splitting of the G peak with lateral resolution, we performed Raman maps. Figure 3 shows spatial Raman maps for a suspended Hall bar indicating the positions of the two split modes  $G^+$  and  $G^-$ , the splitting  $\text{pos}(G^+) - \text{pos}(G^-)$  and the intensity ratio  $I(G^+)/I(G^-)$ . The maps were obtained along the centerline of the device using 785 nm excitation and a pixel resolution of  $0.7 \mu\text{m}$ . It is obvious that not only the G-band splitting, but also the individual positions of the split modes vary strongly across the device. The variation of the positions together with a variation of the intensities suggests significant lateral doping inhomogeneities in the bilayer sample.<sup>28</sup> This finding is similar to that observed in bilayer graphene intercalate produced using ferric chloride.<sup>36</sup> Moreover, these charge variations are corroborated by the magnetotransport measurements presented below.

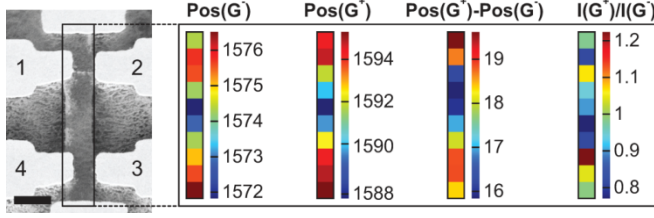


**Figure 3.** Raman maps showing positions of  $G^-$  and  $G^+$  modes ( $Pos(G^-)$  and  $Pos(G^+)$ ), the splitting between the peaks ( $Pos(G^+)-Pos(G^-)$ ) and ratio of integrated peak intensities ( $I(G^+)/I(G^-)$ ) for a FSEG Hall bar device. Maps were produced using a 785 nm excitation, with each pixel corresponding to  $0.7 \mu m$ . Scale bar for SEM image is  $1 \mu m$ .

#### D. Magnetotransport of FSEG

We investigated the transport properties of freely suspended Hall bars under cryogenic vacuum in weak and strong fields using low frequency lock-in techniques. In the weak field regime, the Hall effect charge carrier density  $n_H$  can be calculated from the slope  $R_H$  of the linear trend (cf. Fig. 4(a)) of the Hall resistance  $R_{xy}(B)$ , as  $n_H = 1/R_H e$  (this procedure assumes a homogeneous conductor). We computed a temperature-independent  $n_H \approx 2.5 \cdot 10^{12} \text{cm}^{-2}$  from the Hall resistance measured in two different contact configurations (i.e. contacts 1-2 or 3-4 in Fig. 3). From the longitudinal resistivity  $\rho_{xx}$  (measured either between contacts 2-3 or 1-4 in Fig. 3) an average Hall mobility  $\mu_H = 1/en_H \rho_{xx} \approx 350 \text{ cm}^2/\text{Vs}$  was then calculated.

This rather low mobility value is inconsistent with the occurrence of Shubnikov-de Haas (SdH) oscillations, which were observed for  $B > 4.5 \text{ T}$  in the sample (Fig. 4(a,b)). In Fig. 4(a), the presence of SdH oscillations of low amplitude is masked by a large negative magnetoresistance. After subtracting a smooth background, however, SdH oscillations are clearly visible (Fig. 4(b)). As SdH oscillations can only develop in high-mobility samples in strong fields when  $\mu B > 1$ ,<sup>37</sup>

this implies  $\mu > 2200 \text{ cm}^2/\text{Vs}$  for the sample. The fan diagram for the resistance oscillations is shown in Fig. 4(c). Here the  $1/B$ -positions of the resistance extrema are plotted against their corresponding Landau level (LL) index  $N$  (note that in Fig. 4(c),  $N$  is reduced by 0.5 for the maxima in order to increase the number of points for the subsequent fit). The linearity of the plot confirms that the observed oscillations are indeed SdH oscillations. Furthermore, the density of the high-mobility charge carriers that cause the oscillations may be computed from the slope  $B_0$ , of the fan diagram<sup>38,39</sup> using  $n_{\text{SdH}} = \frac{2e}{\pi h} B_0$ , which yields  $n_{\text{SdH}} \approx 3.3 \cdot 10^{12} \text{ cm}^{-2}$ . This is close to the carrier density obtained from the weak field regime, but implies a mobility of  $270 \text{ cm}^2/\text{Vs}$ , which is too low to give rise to SdH oscillations, as mentioned before. These discrepant values of mobility suggest that the sample is electrically inhomogeneous and comprises domains of high mobility which cause SdH oscillations as well as domains of reduced mobility which give rise to the high resistivity of the FSEG. The occurrence of strong inhomogeneity patterns is in contrast to QF-BLG after hydrogen intercalation. This difference probably arises due to the different temperatures and chemical environments during intercalation and PEC etching. While the former is a high temperature process in a defined ambient, PEC etching is a room-temperature photochemical process in an aqueous solution. Consequently, the graphene may be doped by adsorbates after the  $\text{sp}^3$ -bonds between SiC and buffer layer are broken.

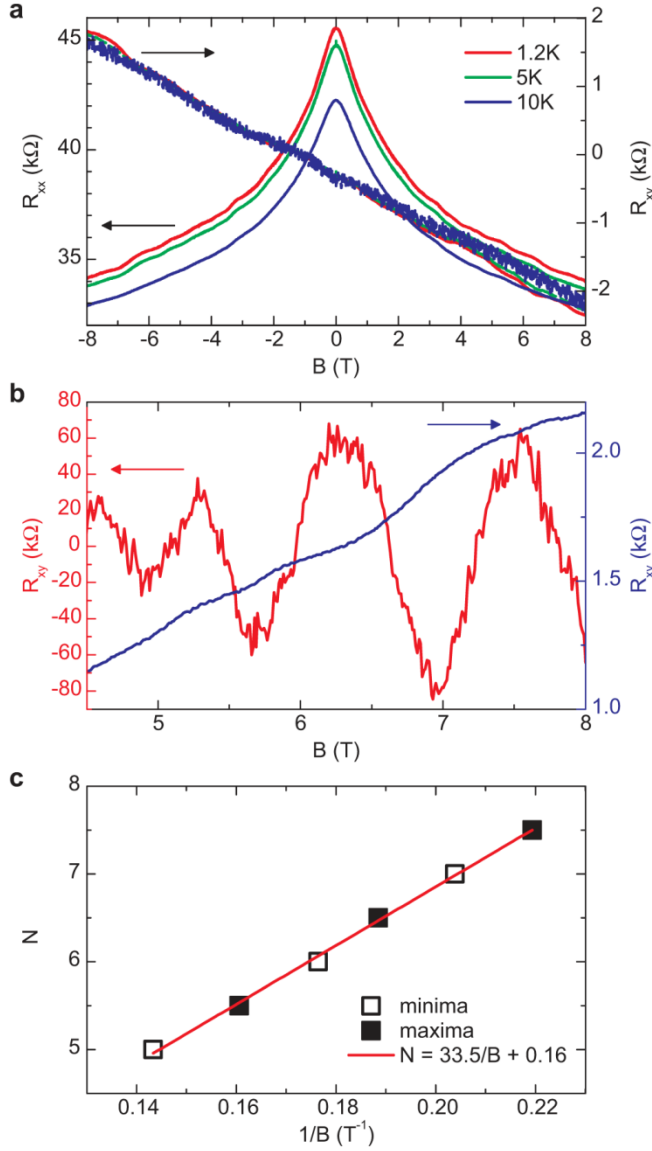


**Figure 4.** (a) The longitudinal resistance  $R_{xx}$  shows a weak-localization peak around  $B = 0$  and an oscillatory behavior at high fields and low temperature. The Hall resistance  $R_{xy}$  is approximately linear and temperature-independent. (b) A zoom to 1.2K data in (a) reveals pronounced Shubnikov-de Haas oscillations in the longitudinal resistance  $\delta R_{xx}$  after a smooth background is subtracted. No conspicuous plateaus are visible in  $R_{xy}$ . (c) The evaluation of the Landau-level index  $N$  of the extrema over their  $1/B$ -positions yields a linear trend (for the maxima  $N$  is reduced by 0.5 in this diagram). The charge carrier density can be calculated from

the slope of this line as  $n \approx 3.3 \cdot 10^{12} \text{cm}^{-2}$ . The axis intercept of  $\beta = 0.16 \pm 0.14$  indicates AB-stacking where  $\beta = 0$  is expected.

In addition to information about the charge carrier density, the fan diagram (Fig. 4(c)) can give insight into the layer number and stacking of the studied graphene material. For bilayer graphene with AB-stacking, an axis intercept of  $\beta = 0$  is expected for the linear trend. Note that for monolayer graphene<sup>40</sup> or decoupled layers<sup>41</sup>,  $\beta = 0.5$  is expected. The observation of  $\beta = 0$  in Fig. 4(c), which corresponds to a Berry phase of  $2\pi$ , thus confirms that the FSEG is indeed AB-stacked bilayer graphene. This finding is in line with recent magnetotransport measurements of QF-BLG created via hydrogen intercalation.<sup>9,10</sup>

#### IV. CONCLUSIONS

In summary, a combination of Raman spectra and magnetotransport data was used to investigate the properties of FSEG structures. Raman spectroscopy and the evaluation of SdH oscillations give convincing evidence that the free-standing structures behave very similar to AB-stacked bilayer graphene. This leads us to conclude that the buffer layer gets converted to a graphene layer during the PEC etching process. The broken inversion symmetry in the bilayer revealed by the Raman data is a consequence of different charges on the top and bottom layers. In addition, spatial Raman maps and magnetotransport data suggest lateral inhomogeneities in the form of domains with different charge carrier concentrations and mobilities. In contrast to high temperature intercalation techniques, the PEC etching process provides a chemical tool for

routine room temperature fabrication of free-standing graphene structures for other scientific explorations.

### **Supplemental Material**

Fabrication process for FSEG devices on insulating SiC and conditions for N and Al implantation; Raman spectroscopy and magnetotransport on FSEG produced from nitrogen implanted (NI) and aluminum implanted (AI) SiC; discussion of the fabrication of suspended nanoribbons by the PEC etch of buffer-layer samples.

### **Corresponding Author**

\*Shriram Shivaraman [ss626@cornell.edu](mailto:ss626@cornell.edu), Johannes Jobst [johannes.jobst@physik.uni-erlangen.de](mailto:johannes.jobst@physik.uni-erlangen.de)

### **Author Contributions**

<sup>§</sup>These authors contributed equally.

### **Acknowledgement**

This work was supported in part by the Cornell Center for Materials Research with funding from the NSF MRSEC program (DMR-1120296) and the AFOSR-MURI (Grant: FA9550-09-1-0705). It was performed in part at the Cornell NanoScale Facility which is supported by the NSF (Grant ECS-0335765). We gratefully acknowledge support within the Cluster of Excellence



‘Engineering of Advanced Materials’ ([www.eam.-uni-erlangen.de](http://www.eam.-uni-erlangen.de)) and the SFB 953 ‘Synthetic Carbon Allotropes’ at the Friedrich-Alexander-Universität Erlangen-Nürnberg.

- 1 K. V. Emtsev, A. Bostwick, K. Horn, *et al*, Nat Mater **8**, 203 (2009).
- 2 C. Riedl, C. Coletti, and U. Starke, Journal of Physics D **43**, 374009 (2010).
- 3 J. M. Dawlaty, S. Shivaraman, J. Strait, P. George, M. Chandrashekhar, F. Rana, M. G. Spencer, D. Veksler, and Y. Chen, Applied Physics Letters **93**, 131905 (2008).
- 4 A. Bostwick, K. V. Emtsev, K. Horn, *et al*, *Photoemission Studies of Graphene on SiC: Growth, Interface, and Electronic Structure*, edited by R. Haug (Springer Berlin Heidelberg, 2008), 47, p. 159.
- 5 A. L. Walter, K. Jeon, A. Bostwick, *et al*, Applied Physics Letters **98**, 184102 (2011).
- 6 I. Gierz, T. Suzuki, R. T. Weitz, *et al*, Phys. Rev. B **81**, 235408 (2010).
- 7 F. Speck, J. Jobst, F. Fromm, M. Ostler, D. Waldmann, M. Hundhausen, H. B. Weber, and T. Seyller, Applied Physics Letters **99**, 122106 (2011).
- 8 M. H. Oliveira Jr., T. Schumann, F. Fromm, R. Koch, M. Ostler, M. Ramsteiner, T. Seyller, J. M. J. Lopes, and H. Riechert, Carbon **52**, 83-89 (2013).

- 9 K. Lee, S. Kim, M. S. Points, T. E. Beechem, T. Ohta, and E. Tutuc, Nano Letters **11**, 3624 (2011).
- 10 S. Tanabe, Y. Sekine, H. Kageshima, and H. Hibino, Japanese Journal of Applied Physics **51**, 02BN02 (2012).
- 11 K. I. Bolotin, K. J. Sikes, Z. Jiang, M. Klima, G. Fudenberg, J. Hone, P. Kim, and H. L. Stormer, Solid State Communications **146**, 351-355 (2008).
- 12 S. Shivaraman, R. A. Barton, X. Yu, *et al*, Nano Letters **9**, 3100 (2009).
- 13 E. McCann, K. Kechedzhi, V. I. Fal'ko, H. Suzuura, T. Ando, and B. Altshuler, Phys. Rev. Lett. **97**, 146805 (2006).
- 14 F. Tikhonenko, A. Kozikov, A. Savchenko, and R. Gorbachev, Phys. Rev. Lett. **103**, 226801 (2009).
- 15 D. Waldmann, B. Butz, S. Bauer, *et al*, ACS Nano Article ASAP; 10.1021/nm401037c
- 16 A. C. Ferrari, Solid State Communications **143**, 47-57 (2007).
- 17 L. M. Malard, M. A. Pimenta, G. Dresselhaus, and M. S. Dresselhaus, Physics Reports **473**, 51-87 (2009).
- 18 C. H. Lui, Z. Li, Z. Chen, P. V. Klimov, L. E. Brus, and T. F. Heinz, Nano Letters **11**, 164 (2011).

- 19 J. Röhr, M. Hundhausen, K. V. Emtsev, T. Seyller, R. Graupner, and L. Ley, *Applied Physics Letters* **92**, 201918 (2008).
- 20 S. Shivaraman, M. V. S. Chandrashekar, J. Boeckl, and M. Spencer, *Journal of Electronic Materials* **38**, 725 (2009).
- 21 M. Huang, H. Yan, C. Chen, D. Song, T. F. Heinz, and J. Hone, *Proceedings of the National Academy of Sciences* **106**, 7304 (2009).
- 22 T. M. G. Mohiuddin, A. Lombardo, R. R. Nair, *et al*, *Phys. Rev. B* **79**, 205433 (2009).
- 23 W. Zhao, P. H. Tan, J. Liu, and A. C. Ferrari, *Journal of the American Chemical Society* **133**, 5941 (2011).
- 24 M. A. Pimenta, G. Dresselhaus, M. S. Dresselhaus, L. G. Cancado, A. Jorio, and R. Saito, *Phys. Chem. Chem. Phys.* **9**, 1276 (2007).
- 25 X. Dong, Y. Shi, Y. Zhao, *et al*, *Phys. Rev. Lett.* **102**, 135501 (2009).
- 26 L. M. Malard, D. C. Elias, E. S. Alves, and M. A. Pimenta, *Phys. Rev. Lett.* **101**, 257401 (2008).
- 27 J. Yan, T. Villarson, E. A. Henriksen, P. Kim, and A. Pinczuk, *Phys. Rev. B* **80**, 241417 (2009).
- 28 P. Gava, M. Lazzeri, A. M. Saitta, and F. Mauri, *Phys. Rev. B* **80**, 155422 (2009).

- 29 T. Ando and M. Koshino, Journal of the Physical Society of Japan **78**, 034709-034716 (2009).
- 30 M. Bruna and S. Borini, Phys. Rev. B **81**, 125421 (2010).
- 31 W. Zhao, P. Tan, J. Zhang, and J. Liu, Phys. Rev. B **82**, 245423 (2010).
- 32 S. S. Lin, B. G. Chen, C. T. Pan, S. Hu, P. Tian, and L. M. Tong, Applied Physics Letters **99**, 233110 (2011).
- 33 A. C. Crowther, A. Ghassaei, N. Jung, and L. E. Brus, ACS Nano **6**, 1865 (2012).
- 34 C. Attacalite, L. Wirtz, M. Lazzeri, F. Mauri, and A. Rubio, Nano Letters **10**, 1172 (2010).
- 35 M. Bruna and S. Borini, Phys. Rev. B **83**, 241401 (2011).
- 36 N. Kim, K. S. Kim, N. Jung, L. Brus, and P. Kim, Nano Letters **11**, 860 (2011).
- 37 S. Datta, *Electronic transport in mesoscopic systems* (Cambridge University Press, Cambridge, UK; New York, 1997).
- 38 K. S. Novoselov, A. K. Geim, S. V. Morozov, D. Jiang, M. I. Katsnelson, I. V. Grigorieva, S. V. Dubonos, and A. A. Firsov, Nature **438**, 197-200 (2005).
- 39 Y. Zhang, Y. W. Tan, H. L. Stormer, and P. Kim, Nature **438**, 201 (2005).
- 40 J. Jobst, D. Waldmann, F. Speck, R. Hirner, D. K. Maude, T. Seyller, and H. B. Weber, Physical Review B **81**, 195434 (2010).

41 C. Berger, Z. Song, X. Li, *et al*, Science **312**, 1191 (2006).